

High seismic velocity structures control moderate to strong induced earthquake behaviors by shale gas development

Junlun Li^{1,2,3✉}, Jian Xu¹, Haijiang Zhang^{1,2,3✉}, Wen Yang¹, Yuyang Tan⁴, Fengshou Zhang⁵, Lingyuan Meng⁶, Yang Zang⁶, Siyu Miao¹, Chang Guo¹, Zhenyue Li¹, Renqi Lu⁷ & Jianbao Sun⁷

Moderate to strong earthquakes have been induced worldwide by shale gas development, however, it is still unclear what factors control their behaviors. Here we use local seismic networks to reliably determine the source attributes of dozens of $M > 3$ earthquakes and obtain a high-resolution shear-wave velocity model using ambient noise tomography. These earthquakes are found to occur close to the target shale formations in depth and along high seismic velocity boundaries. The magnitudes and co-seismic slip distributions of the 2018 Xingwen $M_L 5.7$ and 2019 Gongxian $M_L 5.3$ earthquakes are further determined jointly by seismic waveforms and InSAR data, and the co-seismic slips of these two earthquakes correlate with high seismic velocity zones along the fault planes. Thus, the distribution of high velocity zones near the target shale formations, together with the stress state modulated by hydraulic fracturing controls induced earthquake behaviors and is critical for understanding the seismic potentials of hydraulic fracturing.

¹Laboratory of Seismology and Physics of Earth's Interior, School of Earth and Space Sciences, University of Science and Technology of China, 96 Jinzhai Road, Hefei 230026 Anhui, China. ²Mengcheng National Geophysical Observatory, University of Science and Technology of China, Hefei, Anhui, China. ³CAS Center for Excellence in Comparative Planetology, University of Science and Technology of China, 96 Jinzhai Road, Hefei 230026 Anhui, China. ⁴Frontiers Science Center for Deep Ocean Multispheres and Earth System, Key Lab of Submarine Geosciences and Prospecting Techniques MOE, College of Marine Geosciences, Ocean University of China, Qingdao 266100 Shandong, China. ⁵Department of Geotechnical Engineering, College of Civil Engineering, Tongji University, Shanghai, China. ⁶China Earthquake Networks Center, Beijing, China. ⁷State Key Laboratory of Earthquake Dynamics, Institute of Geology, China Earthquake Administration, Beijing, China. ✉email: lijunlun@ustc.edu.cn; zhang11@ustc.edu.cn

It is known that seismicity can be induced by hydraulic fracturing (HF) for shale gas development due to pore pressure changes in the preexisting faults, poroelastic stress changes caused by high-pressure fluid injections and aseismic slip loading on unstable faults^{1–12}. Extensive studies on the recent seismicity induced by HF and waste water disposal in the western Canada and central US have been conducted by analyzing seismicity source attributes, correlating seismicity with water injection schedules, modelling stress perturbations by water injection process, and conducting seismic surveys on preexisting faults^{3,9,13–19}. It has been suggested that the HF volume is closely associated with induced earthquake productivity for small earthquakes in the Duvernay play, Canada⁹. For moderate to strong earthquakes, it was previously found that magnitudes of induced earthquakes are proportional to the injection volume²⁰, which was then modified by incorporating rupture physics of earthquakes induced by pore-pressure perturbations²¹. However, late studies found that these estimations of the magnitude bounds are not applicable to the fluid-injection-induced earthquakes, including the 2017 Mw5.5 Pohang earthquake²², the 2014 M4.4 and 2015 M4.6 earthquakes near Fort St. John, Canada¹⁶, where the dimension of a fault in the critical state of stress is considered as the controlling factor for the maximum magnitude, rather than the injection volume. Recently, an alternative approach was proposed to predict the exceedance probability of an assumed magnitude of a potential induced earthquake by calculating the time-varying seismogenic index²³. Though their method can be applied to predict the significant probability of the Pohang Mw5.5 earthquake, the maximum magnitude, which is a key parameter in their prediction is controlled by local tectonic features and is not known a priori. Although attempts have been made to map detailed fault systems to discern the potential seismogenic structures in the unconventional shale gas field in western Canada and the central US^{24–27}, it has been widely observed that many preexisting faults, particularly those strike-slip faults which are reactivated during HF, could not be identified by 3-D seismic imaging likely due to lack of distinct throw^{17,26,28}.

Compared to shale gas fields in western Canada and the central US, more moderate and strong earthquakes have been induced in southern Sichuan basin, especially in the Changning-Zhaotong (C-Z) field (Fig. 1; Supplementary Fig. 1). In this region, the historical earthquake activity was relatively low⁵. However, with the massive production of shale gas since 2014, occurrence of small to moderate to strong earthquakes has increased abnormally^{5,29–33} (Fig. 1c), including the devastating Xingwen M_L 5.7 earthquake on 16 December, 2018 and the Gongxian M_L 5.3 earthquake on 3 January, 2019³⁴. Should the 2018 Xingwen M_L 5.7 earthquake indeed be related to shale gas HF, it would be the largest HF-induced earthquake in the world^{34,35}.

Therefore, the C-Z field provides an opportunity to study the factors controlling the distributions and magnitudes of moderate to strong earthquakes induced by HF in this region where the background differential stress controlled by the southeastern tectonic compression of the Chuandian block against the Sichuan Basin is rather high ($\Delta\sigma > 10\text{MPa}$)^{5,31}. Many recent studies indicate that HF is most likely responsible for inducing or triggering those earthquakes as a result of reactivation of preexisting faults due to fluid migration into faults or the poroelastic stress perturbations caused by hydraulic fracturing process^{5,30,32–34,36}. However, because of the limited access of hydraulic fracturing dataset and the lack of detailed subsurface structures, it remains unclear what controls the occurrence of moderate to strong earthquakes in the C-Z shale gas field. In addition, due to poor depth constraint for some moderate to strong earthquakes including the 2018 Xingwen earthquake in the catalog of the China Earthquake Administration, some studies argue against

relating them with HF based on the observations that they occur far below the target shale formation³⁷.

To unravel the key factors controlling the occurrence of moderate to strong earthquakes, and assess the seismic-prone zones and potential risks in the C-Z field, in this study we take advantage of a dense seismic network to better determine earthquake locations and high-resolution subsurface structure of the field. Also, the detailed regional velocity variations are correlated with moderate to strong earthquake behaviors including rupture initiation and coseismic slip distribution for induced seismicity.

Results and discussion

Geological settings of the C-Z field. The C-Z shale gas field located at the southern margin of the Sichuan basin is one of the three unconventional plays (Changning-Zhaotong, Weiyuan and Fuling) in the Sichuan basin (Figs. 1a, b), which is adjacent to the eastern Qinghai-Tibetan plateau^{36,38}. Situated within the inter-junction area among the Huaying Shan fold belt, the Daliang Shan and the Dalou Mountain fault-fold belts, the C-Z shale gas field suffered from multi-stage tectonic deformations since the Indosinian period^{36,37}. The Jianwu syncline, the Luochang syncline and the Changning anticline which are the three major tectonic structures in this area exhibit distinct surface exposures from the Cambrian to the Cretaceous periods. The C-Z shale gas field is situated in the Jianwu syncline (Fig. 1d), where the stratigraphy contains Sinian (late Proterozoic) to Triassic sediments³⁷ (Fig. 1e).

For shale gas development in this field, there are two target formations including the shallower Wufeng-Longmaxi (late Ordovician to early Silurian) deposited at approximately 2.0 km in depth below mean sea level (MSL) with a 20 m thick sweet-spot interval³⁹, and the deeper Qiongzhusi formations (Early Cambrian) deposited at approximately 4.0 km³⁷ (Fig. 1e). Currently, only the Wufeng-Longmaxi shale formations of marine facies is under production by systematic hydraulic stimulations with dense platforms. The current orientation of the maximum horizontal compressional stress SH_{\max} is $\sim 107^\circ$ ⁴⁰ (Fig. 1d) and the horizontal differential stress exceeds 10 MPa⁵. In this historically seismic quiescent C-Z area, moderate to strong earthquakes have become quite common in the past few years as HF grew consistently (Fig. 1c). More specifically, the number of moderate to strong earthquakes with magnitude larger than M_L 3.0 in the C-Z area has reached 53 from 1 Jan., 2015 to 3 Jan., 2019, including two damaging events with magnitude larger than M_L 5.0.

3D shear velocity model of the C-Z field from ambient noise tomography. Using the two-phased dense arrays deployed in the C-Z shale gas field from 28 Feb. to 6 May, 2019 with portable nodal stations (Fig. 1, method), we have obtained high-quality cross-correlation functions among stations for ambient noise tomography (ANT) (see Methods, Supplementary Figs. 2–6). The periods of the extracted fundamental mode surface waves range from 0.5 s to 5.0 s (Supplementary Fig. 2), and the regional 3-D S-wave velocity structure is obtained down to 5 km in depth from the surface (Fig. 2), with a horizontal spatial resolution of about 2 km (see Methods, Supplementary Fig. 4) and an uncertainty less than 0.05 km/s (see Methods, Supplementary Fig. 5). Therefore, the velocity model used for interpreting the earthquake ruptures and geological susceptibility should be reliably determined in this study.

It is obvious that the Jianwu syncline (Figs. 1, 2) which is composed mainly of Silurian shale and mudstone formations at the depth of ~ 2 km exhibits relatively lower velocity anomalies in

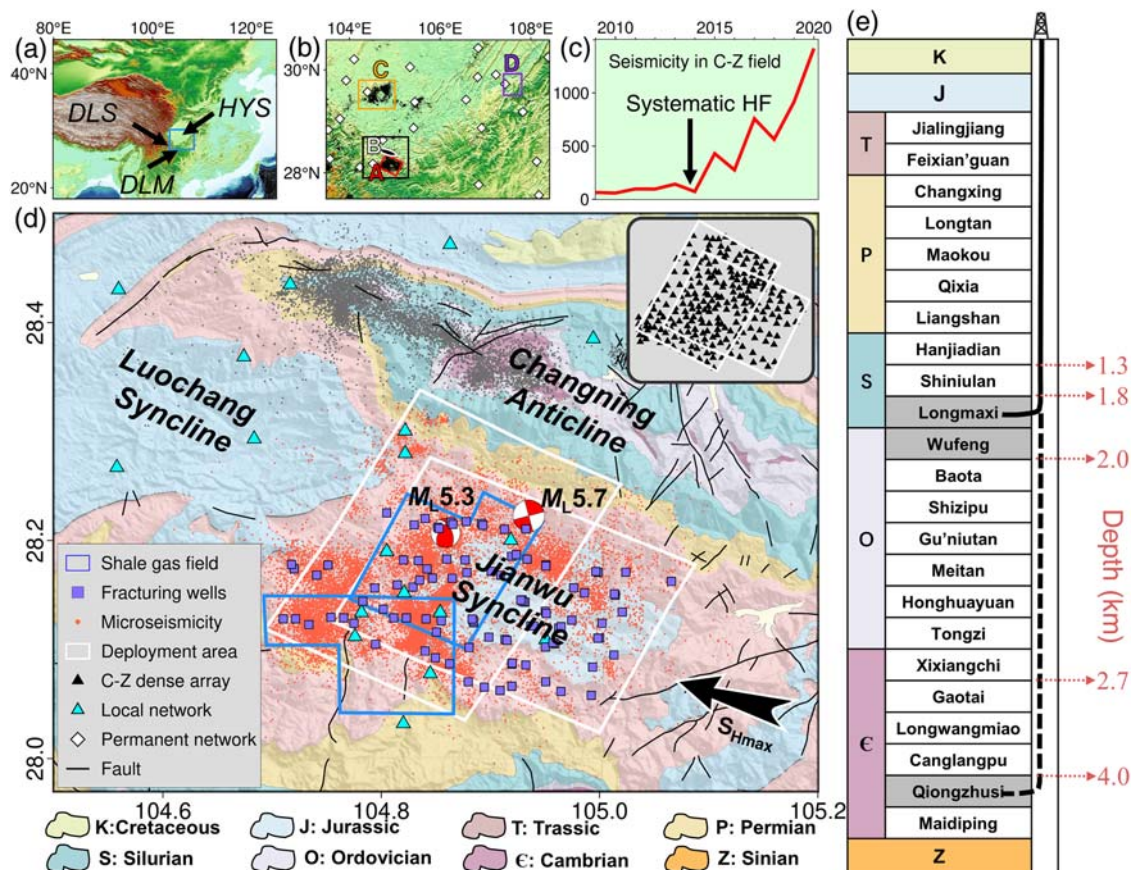


Fig. 1 Seismicity distribution and geological settings. **a** Geographic location of the southern Sichuan Basin. DLS: the Daliang Shan, DLM: the Dalou Mountain, HYS: Huaying Shan. **b** The three shale gas fields (A: Changning-Zhaotong; C: Weiuyan; D: Fuling) and a salt mine (B: Changning) in the Sichuan Basin. The white rhombuses indicate the permanent stations of the Chinese Seismic Network. The area in the black box is further expanded in **(d)**. **c** Increasing number of earthquakes with $M > 1$ in the Changning-Zhaotong field recorded by the Chinese Seismic Network. **d** Surface geology of the Changning-Zhaotong area with the geologic periods denoted by the bottom legends. The two irregularly shaped blue boxes represent the Changning block (north) and the Zhaotong block (south) for shale gas development, and the violet squares represent the hydraulic fracturing well pads in this region. The two white boxes show the coverage of the two-phased seismic dense arrays detailed in the top-right inset. The cyan triangles represent the local network. The orange and gray dots represent the seismicity monitored by the local network (orange for seismicity in the shale gas field and gray for seismicity in the salt mining field) between 1 Feb., 2015 and 31 Dec., 2020. The two beachballs mark the Xingwen $M_L 5.7$ earthquake (16 Dec., 2018) and the Gongxian $M_L 5.3$ earthquake (3 Jan., 2019), respectively. **e** Stratigraphic sequences and target layers for shale gas development in the C-Z field.

general compared to the surrounding formations. In the map view, the outline of the synclinal structure from the surface geology³⁶ correlates well with the velocity heterogeneities (Fig. 2b). In the sectional view, the overall synclinal structure of the inverted model also agrees well with the seismic reflection profile³⁷ (Fig. 3d). Furthermore, the Wufeng-Longmaxi horizon situated at the bottom of this low-velocity anomaly becomes disrupted near the southern end of the 2D reflection profile (distance < 8 km), where the inverted velocity model from ANT also varies noticeably, indicating a lithology change as the low-velocity silt shale formation terminates. The consistency between the active- and passive-source seismic results supports the reliability and accuracy of the inverted velocity model.

Earthquake locations and focal mechanisms in the C-Z field.

Using the continuous data from the local network consisting of 21 stations (Cyan triangles in Fig. 1) which started to operate since 2015³⁰, the hypocenters of 53 $M_L 3.0+$ earthquakes occurring between 1 Jan., 2015 and 3 Jan., 2019, and 4 $M_L 4.0+$ between 3 Jan., 2019 and 31 Dec., 2021 are carefully relocated with manually picked arrival times (see Methods, Supplementary Fig. 7). The source mechanisms of these earthquakes are determined using a full waveform matching method (see Methods,

Supplementary Fig. 8). Uncertainty analyses by bootstrapping tests are conducted to evaluate the reliability of these source mechanisms. The inverted source mechanisms show high consistency for most earthquakes (See methods, Supplementary Fig. 9). Furthermore, surface wave amplitude analyses^{5,41} are also performed to validate the shallow centroid depths of the Xingwen $M_L 5.7$ and Gongxian $M_L 5.3$ earthquakes. It is found that the centroids of both earthquakes are situated within the depth range of 1 km to 3 km, consistent with the resolved depths from the source mechanism inversion (See methods, Supplementary Fig. 10).

We find that most of these earthquakes are located close to the velocity boundaries or within high-velocity zones around the syncline (Fig. 2), with the majority of the focal depths located within the brittle dolomite and anhydrite rocks between the W-L and Qiongzhusi shale formations shallower than 4 km (Supplementary Fig. 11). Also, the dominant NNW or the conjugated NEE strikes (Supplementary Fig. 12) are consistent with the slip tendency proposed by Lei et al.³² and the regional tectonic stress direction from the world stress map⁴⁰ (Fig. 1).

We also manually processed about 26,000 microearthquakes (Set A) recorded by the local network during 1 Jan., 2015 and 31 Dec., 2020, and about 8000 microearthquakes (Set B) recorded by

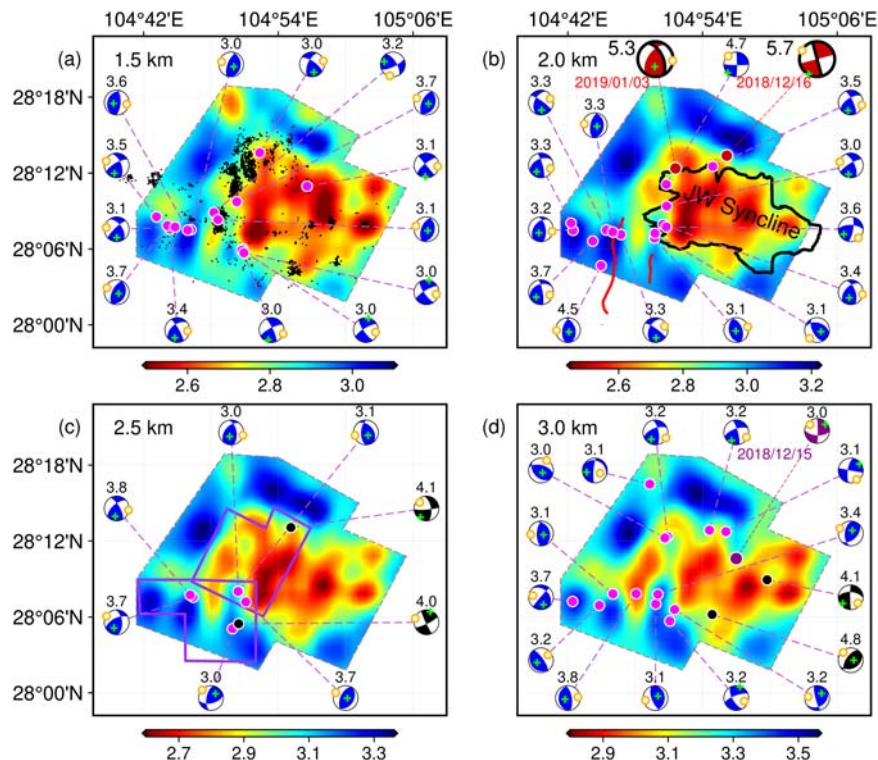


Fig. 2 Shear wave velocity model and source mechanisms. Velocity slices shown at four depths 1.5 km, 2 km, 2.5 km and 3 km (mean sea level, MSL). The source mechanisms for those events occurring between 2015 and 2019 with $M_L > 3.0$ (blue beachballs with magenta epicenters), and of those between 2019 and 2022 with $M_L > 4.0$ (black) are shown accompanied by the compressional and tensional axes. The determined depths of the source mechanisms projected to the individual velocity slices are 0–1.75, 1.75–2.25, 2.25–2.75, 2.75–4 km, respectively. In panel (a), s recorded by the two-phased dense arrays from 28 Feb., 2019 to 6 May, 2019. In panel (b), the black curve outlines the Jianwu syncline adapted from Lu et al. (2021)³⁶, and the red lines indicate the known faults identified from surface traces. In panel (c), the purple boxes indicate the Changing-Zhaotong shale gas field. In panel (d), the beachball in purple represents the foreshock of the Xingwen $M_L 5.7$ earthquake.

the two-phased dense arrays (black triangles in the upper-right inset in Fig. 1d) over the 70-day period (see Methods). The distribution of the microearthquakes with magnitude less than $M_L 0$ exhibit no distinct spatial difference between areas adjacent to and away from the HF wellheads (Supplementary Fig. 13), suggesting that the detection of microseismic events inside the fluid-injection areas is not obviously biased by the surface industrial noise for those events with magnitudes above $M_L - 1$ considered in this study. The local events in Set A shallower than 4 km coincide with the flank of the syncline with large velocity contrast (Supplementary Fig. 14). Seismic events in Set B are better constrained in depth by the two-phased dense arrays, and mainly consist of four swarms at distinct depths with magnitudes ranging from $M_L - 1$ to $M_L 3.7$ (Fig. 4). The two moderate earthquakes with magnitude above $M_L 3.0$ in Set B are located below the W-L target formation, nucleating at about the same depth as the Gongxian $M_L 5.3$ earthquake (Fig. 4d). These two moderate earthquakes are also recorded by part of the local network but are located deeper than the depths determined by the dense arrays due to larger uncertainties in focal depth by the sparse network (see Methods, Supplementary Fig. 15). The discrepancy in focal depths determined by those two seismic networks indicates that the dense arrays can improve the accuracy of the focal depths with more S-arrivals recorded by stations within 1.4 times the distance of the focal depth⁴².

The four relocated swarms of seismicity (Fig. 4d), namely Groups A, B, C and D, occur in different strata with distinct lithology, including the W-L shale formation (the target stratum), the Shiniulan sandy mudstone formation and the Xixiangchi dolomite formation, respectively. Groups A and B may be directly

associated with hydraulic fracturing since they are concentrated in the injection depths. In comparison, Groups C and D are situated in the upper sandstone and the lower dolomitic formations with respect to the target W-L shale formation, respectively, which have higher seismic potentials due to their velocity-weakening properties⁴³. Groups C and D may be triggered by the stress perturbations induced by multistage HF operations⁴³ or fluid propagation into preexisting faults along hidden conduits characterized by the microearthquake migration footprints (red arrow in Fig. 4d). The distribution of seismicity reveals not only the definite link between HF and induced seismicity, but also the seismic potential of certain strata in proximity to the fluid-injection locales.

Source attribute characterization of the 2018 Xingwen $M_L 5.7$ earthquake. The 2018 Xingwen $M_L 5.7$ earthquake struck the C-Z shale gas field on 16 Dec., 2018 and resulted in significant damages and losses to the local infrastructures³⁴. With more accurate velocity models (see Methods) and more accurate arrival times from the local network (see Methods), it is relocated at latitude of 28.223°, longitude of 104.835°, and depth of 3.0 km, much shallower than the depth of 12 km from the CEA catalog. The nearby well pad N201H24 (Fig. 3, Supplementary Fig. 1), which is about 1.0 km away from the initiation point (epicenter) of the Xingwen $M_L 5.7$ earthquake, was in hydraulic fracturing or shut-in operations (started in Oct. 2018) when the major earthquake occurred³⁴. The foreshock and aftershock patterns of the Xingwen $M_L 5.7$ mainshock exhibits similar spatial-temporal features with the 2017 $M_w 5.5$ Pohang earthquake^{44,45}. For the

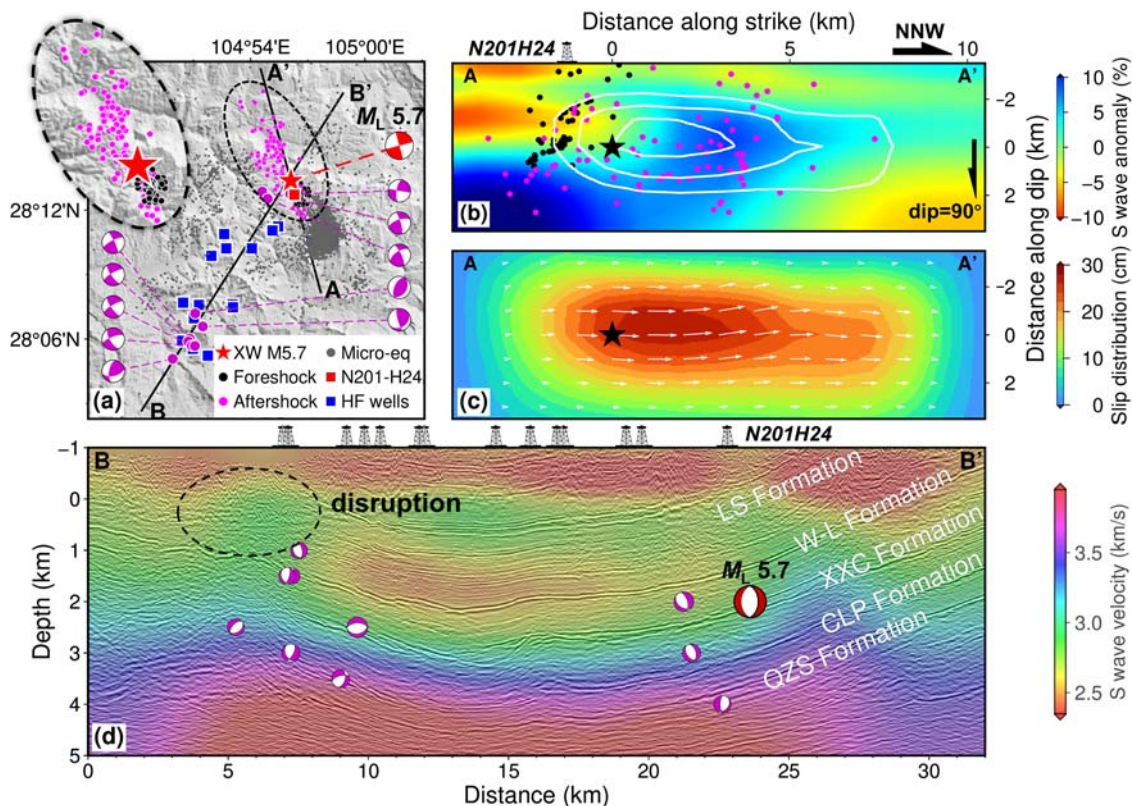


Fig. 3 Source attribute analysis for the Xingwen M_L 5.7 earthquake. **a** The Xingwen (XW) M_L 5.7 earthquake sequence monitored by the local network within 40 days from 26 Nov., 2018 to 6 Jan., 2019. The top left elliptical inset shows the zoomed-in spatial pattern of the fore-main-aftershocks, and the black and magenta dots represent foreshocks and aftershocks, respectively. The gray dots denote more distant induced seismicity. The blue squares mark the hydraulic fracturing well pads close to line BB' with the N201H24 well pad highlighted by red. The magenta beachballs represent the moderate earthquakes close to the line BB'. **b** The velocity anomaly profile along the rupture plane shown as line A-A' in (a). The initiation point is indicated by the black star, and the main slip areas are enclosed by the white dashed lines. The black and magenta dots indicate the foreshocks and aftershocks within 1 km in distance to the rupture plane AA'. The origin of the cross-section is referenced to the initiation point and the anomaly is referenced to the average velocity at each depth. The locations of the HF platforms close to line AA' are plotted on top. **c** The distribution of the co-seismic slips from the finite-fault rupture inversion (see Methods) along the same fault plane in (b). **d** Comparison between the 2-D active source seismic profile (39) with the shear velocity model from ANT. The major stratigraphic layers are marked. The depths of the lithological sequence are determined by well N203³⁷. The locations of the HF platforms close to line BB' are plotted at the top of panel (d).

Xingwen earthquake, a few foreshocks concentrated to the southeast of the mainshock and finally led to the mainshock. The distribution of the numerous aftershocks clearly delineates the rupturing plane along a previous unknown fault trending in the NNW-SSE direction (Fig. 3a). In addition, along the rupturing plane there exists a local velocity contrast striking in the same direction, suggesting the existence of a preexisting fault or a weak zone accommodating this earthquake (Fig. 2). Using the finite-fault rupture inversion method with data recorded by the permanent stations in proximity (Method, Supplementary Figs. 16–18), we more accurately determine the rupturing process of the Xingwen M_L 5.7 earthquake (Fig. 3c; Supplementary Fig. 16). Some large-amplitude shear waves at stations in close proximity to the epicenter are carefully reconstructed using the projection onto convex sets (POCS) method⁴⁶ (Method). The similarities of seismograms before and after the reconstructions in both waveforms and spectra suggest that the reconstruction should be reliable (Supplementary Fig. 17). The main slip area is well associated with a high-velocity anomaly zone along the fault plane (Fig. 3), which is geomechanically stronger and can accumulate more stresses compared to surrounding areas^{47–49}, and potentially acts as an asperity for developing strong earthquakes. Similar to the Xingwen M_L 5.7 earthquake, the Gongxian M_L 5.3 earthquake also nucleated at the boundary between the high and

low velocities, and propagated unilaterally into the high-velocity anomaly zone, which acts as an asperity for the strong earthquake. The inverted finite-fault slip distribution and the associated high-velocity asperity (5 km by 3 km) correlate well with the rupture area of $\sim 17 \text{ km}^2$ calculated with the empirical formula between magnitude and rupture area⁵⁰.

Our high-resolution model reveals the Xingwen M_L 5.7 earthquake nucleated at the velocity boundary or along a preexisting fault, however, it is not imaged in the active-source reflection profile (Fig. 3d), likely due to lack of significant throw or horizontal dislocations³⁶. Therefore, the high-resolution velocity structure is found to be critical for identifying the seismogenic zones in the C-Z field.

It is noteworthy that a moderate M_L 3.0 earthquake with a rather similar source mechanism occurred on 15 Dec., 2018, only one day prior to the Xingwen M_L 5.7 earthquake at about 5 km to the southeast (Fig. 2d). The two strike-slip events seem to rupture on the same fault trending in the NNW-SSE. It is intriguing whether the M_L 3.0 moderate earthquake triggered the Xingwen M_L 5.7 earthquake. Though the Coulomb stress change caused by the M_L 3.0 earthquake (Supplementary Fig. 19) is positive where the Xingwen M_L 5.7 nucleates, it is probably too insignificant ($< 10^{-4} \text{ MPa}$) to be an effective triggering factor (see Methods)^{4,5}.

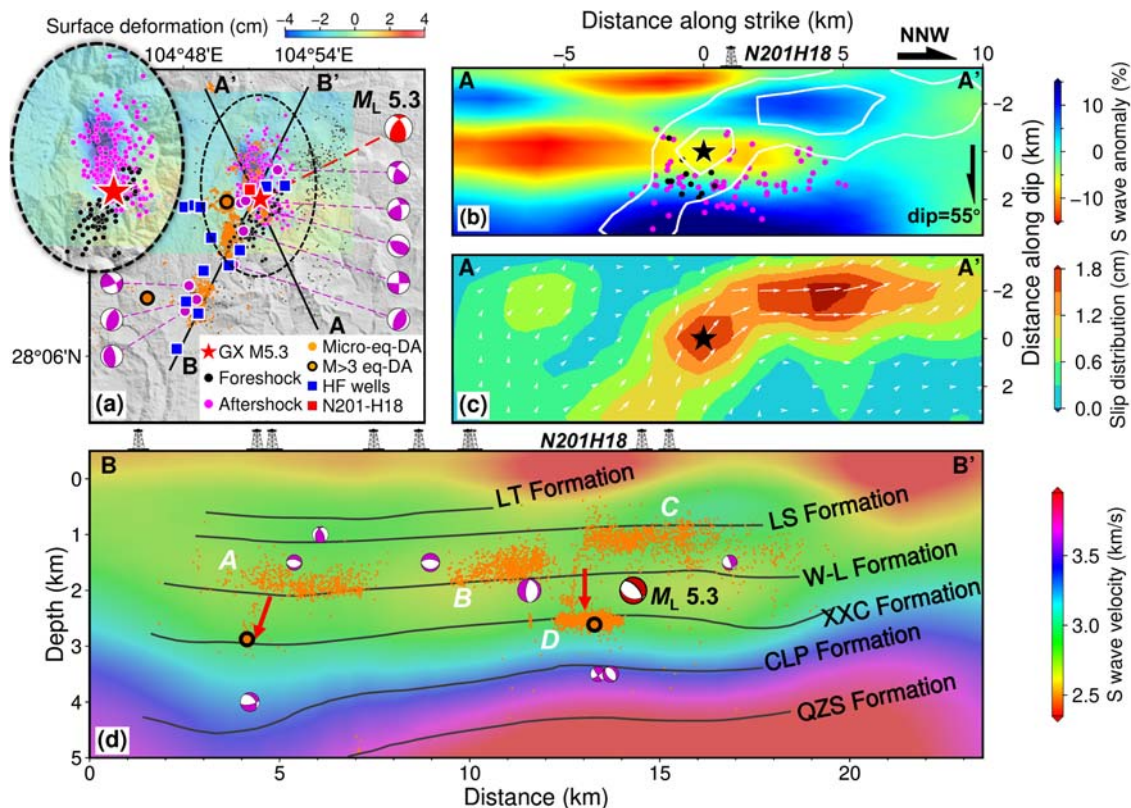


Fig. 4 Source attribute analysis for the Gongxian M_L 5.3 earthquake. **a** The Gongxian (GX) M_L 5.3 earthquake sequence monitored by the local network in a period of 40 days from 13 Dec., 2018 to 31 Jan., 2019 with surface deformation from InSAR (colored area). The top left elliptical inset shows the zoomed-in spatial pattern of the fore-main-aftershocks, and the black and magenta dots represent foreshocks and aftershocks, respectively. The orange dots denote the seismicity monitored by the two-phased dense arrays (DA) between 28 Feb. 2019 and 8 May. 2019 with the two $M_L > 3.0$ earthquakes highlighted by larger solid circles. The blue squares mark the hydraulic fracturing well pads close to line BB' with the N201H18 well pad highlighted by red. The magenta beachballs represent the moderate earthquakes close to the line BB'. **b** The velocity anomaly profile from ANT along the rupture plane (the dip angle is 55°) shown as line A-A' in **(a)**. The initiation point is indicated by the black star, and the main slip areas are enclosed by the white dashed lines. The black and magenta dots indicate the foreshocks and aftershocks within 1 km in distance to the rupture plane AA'. The HF platforms close to line BB' are plotted on top. **c** The distribution of co-seismic slips by the finite-fault rupturing model. **d** Comparison between the 2-D active source seismic profile with the shear velocity model from ANT, where the major stratigraphic sequence boundaries are inferred from well N201³⁷ and discussions with local operators. The orange dots and black circles represent the microseismicity and $M_L > 3.0$ earthquakes monitored by the dense arrays, respectively. The red arrows infer the possible fluid conduits characterized by the linearly distributed microseismicity. The HF platforms close to line BB' are plotted at the top of panel **(d)**.

Source attribute characterization of the Gongxian M_L 5.3 earthquake. The Gongxian M_L 5.3 earthquake occurred on 3 Jan., 2019, while the nearby N201H18 well pad (Fig. 4, Supplementary Fig. 1) started hydraulic fracturing in December, 2018 and continued hydraulic fracturing or shut-in operations when this earthquake occurred³⁴. This earthquake is located at latitude of 28.206° , longitude of 104.859° , depth of 2.3 km, and is close to the target shale formation using accurately picked arrival times recorded by the local network (Supplementary Fig. 7), which is also much shallower than the depth of 15 km in the CEA catalog. Similar to the Xingwen earthquake, the foreshocks are also concentrated to the southeast of the nucleation point, while the aftershocks are distributed to the opposite direction of the mainshock, characterizing unilateral NNW rupturing (Fig. 4a). Moreover, the surface deformation from InSAR shows a distinct uplift in the NW direction (A'-A), consistent with the reverse faulting mechanism with a strike-slip component (Fig. 4a). The local velocity contrast also shows a clear strike in the same NW direction, suggesting that the earthquake occurred on a pre-existing lithological boundary. The NNW-trending rupture determined by the velocity contrast, the surface deformations as well as the aftershock distributions correlates well with a surface gully of a similar unilateral strike (Supplementary Fig. 20). This

high correlation between earthquake rupturing characteristics and surface topographic features suggests that the reverse fault accommodating the Gongxian M_L 5.3 earthquake could also be revealed by the surface gully, which may provide a complementary approach for identifying shallow blind faults in this region.

Using the finite-fault rupture inversion method constrained by both the seismic and InSAR data (see Methods), the coseismic slip distribution is clearly associated with the high-velocity anomaly zone along the fault strike (Fig. 4). Similar to the Xingwen M_L 5.7 earthquake, the Gongxian M_L 5.3 earthquake also nucleated at the boundary between the high and low velocities, and propagated unilaterally into the high-velocity anomaly zone, which acts as an asperity for the strong earthquake. The high-velocity asperity terminates around $X = 6$ km along the A-A' profile in Fig. 4b, where the rupturing probably is also terminated prematurely, indicating that the high-velocity structure controls on the rupturing process of the Gongxian M_L 5.3 earthquake. The smaller asperity (4 km by 2 km) could be the reason for the smaller magnitude of Gongxian M_L 5.3 earthquake compared to the Xingwen M_L 5.7 earthquake (5 km by 3 km). Thus, high-velocity anomalies along the fault plane act as asperities for induced moderate to strong earthquakes, and their sizes

determine the induced earthquake magnitudes (Fig. 3b and Fig. 4b). Based on the empirical relationship⁵⁰, for the Gongxian earthquake, the rupturing of the high-velocity asperity (4 km by 2 km) would result in an earthquake of M_w 5.0, close to M_w 5.1 as estimated from the finite-fault inversion, and for the Xingwen earthquake, the rupturing of the high-velocity asperity (5 km by 3 km) would result in an earthquake of M_w 5.2, also close to M_w 5.5 as estimated from the finite-fault inversion. The major rupturing areas of the Xingwen M_L 5.7 and Gongxian M_L 5.3 earthquakes are observed to propagate significantly outside the stimulated volumes characterized by the seismicity (Figs. 3 and 4), indicating these two events are runaway earthquakes according to Galis et al. (2017) and Shapiro et al. (2021)^{21,23}. If these two earthquakes were self-arrested within the stress-perturbed areas near the HF wells, they could not rupture through the entire high-velocity asperities and the magnitudes would be much smaller than what have been observed.

The similar foreshock and aftershock behaviors of the Gongxian and Xingwen earthquakes indicate that the two strong earthquakes are likely induced by the same mechanism of pore pressure increase in the preexisting fault zones by the injection fluids migrated into the mainshock areas. It is noted there are two spatially separated $M_L > 3.0$ earthquakes monitored by the two-phased dense arrays within the microearthquake clouds (Orange solid circles in Fig. 4d). There are fluid conduits clearly indicated by linearly distributed seismicity connecting the shallower target shale formation and the two $M_L > 3.0$ earthquakes located below (Fig. 4d), suggesting that those are induced/triggered earthquakes caused by fluid migration. Such triggering behavior associated with downward migrated injection fluid along near vertical faults is also observed in waste water injection-induced earthquakes in the central US and HF-induced earthquakes in southern Alberta, Canada^{27,51}.

Seismic potentials in the Changning shale gas field. With the continuous development of shale gas in the C-Z field, many moderate to strong earthquakes have occurred between 2015 and 2019 in close proximity to the HF well pads, exhibiting spatial and temporal association with HF. Most of those events including the two damaging earthquakes nucleated below the W-L shale formation (Supplementary Fig. 11). This indicates that the formations mainly composed of dolomites and gypsum-rich rocks³¹ between the W-L and Qiongzhusi shale formations have higher seismic potentials than the shallower ductile layers mainly composed of shale and mudstone. This observation is also supported by the laboratory results^{52,53} who found that the carbonate and anhydrite rocks are more prone to seismic slip.

The uneven distribution of the induced seismicity compared to the evenly distributed HF wells (Fig. 1) suggests that the flanks of the JW syncline exhibit higher geological susceptibility to induced earthquakes, correlating well with the areas with large velocity contrasts in our velocity model. Figure 2 shows that not only the majority of the moderate to strong earthquakes are situated around the velocity boundaries, but also many of those earthquakes have their fault planes closely parallel with north to northwest strikes of these boundaries. Given that the maximum horizontal stress (SH_{max}) in this region is oriented in WNW-ESE ($\sim 107^\circ$) and the horizontal differential stress exceeds 10 MPa^{31,54}, preexisting faults or weak zone trending north to northwest are prone to reactivation based on the estimated slip tendency (see Methods, Supplementary Fig. 12). For the two damaging Xingwen and Gongxian earthquakes, their initiation points, slip distributions and magnitudes are well correlated with high-velocity anomalies along the fault plane, indicating the structural control on the occurrence of moderate to strong

earthquakes. Because of the limited access to the hydraulic fracturing data, we cannot check the direct relationship between earthquake productivity and magnitudes with injection volumes. However, the Xingwen and Gongxian earthquakes are found to nucleate in the areas with relatively large velocity contrasts and then propagate into high-velocity regions outside the stimulated volumes, suggesting that these two earthquakes are runaway ruptures like the 2017 Pohang M_w 5.5 earthquake²³, and their magnitudes are likely controlled by high-velocity asperities along the fault planes.

The correlation between seismic velocity anomalies and various earthquake behaviors were also previously observed in continental faults and megathrust faults^{55–58}. For induced events, it was found that major induced earthquakes due to waste water disposal in Oklahoma, central United States occurred either close to the velocity boundaries or within high velocity anomalies in the basement⁵⁹, and the induced earthquakes due to shale gas hydraulic fracturing in Alberta, Canada are spatially associated with the margins of Swan Hills Formation inferred from local geology⁶⁰. Nevertheless, these studies did not examine the coseismic distributions of moderate to strong earthquakes and the correlation of their magnitudes with high-velocity anomalies along the fault planes due to the lack of a detailed shear wave velocity model in their studies. In comparison, in the C-Z shale gas field the correlation between velocity anomalies and earthquake behaviors is better resolved owing to higher resolution of the velocity model from ANT (see resolution test in Supplementary Fig. 4). Therefore, we can further infer susceptible areas for potential strong earthquakes in the C-Z field that could be induced by hydraulic fracturing process based on distribution of high-velocity anomalies. We propose areas susceptible to strong earthquakes should be located between the relatively high and low-velocity anomalies (Fig. 5), where lithological changes and weak zones are prone to slip under shear stress perturbations or effective normal stress changes^{12,61}. The estimated zones of high geological susceptibility in the southeast region of the C-Z field possess higher seismic potentials as the development now moves southeastward along the Jianwu syncline outside the initial C-Z shale gas demonstration areas (Supplementary Fig. 1), with many well pads to be built and drilled^{32,36}. Recently, four moderate events with $M_L > 4.0$ occurred in the C-Z field after 2019 (Fig. 2) are located in the proposed susceptible areas (Fig. 5, Supplementary Fig. 21), corroborating the proposed model for evaluating geological susceptibility.

Therefore, operators in this region should be more conservative in HF operations close to the susceptible regions. The conservativeness in operations may include reducing injection volumes, lowering the injection pressures, shortening horizontal wells, restricting the thresholds for the traffic light protocol, or their combinations. Also, the local operators can better predict the maximum magnitudes of possible induced earthquakes at a specific site and determine the associated seismic potentials by simply calculating the sizes of the high-velocity asperities along the fault planes characterized by the 3-D tomographic model at regions highlighted by the susceptibility map, in conjunction with the fault slip tendency (Supplementary Fig. 12). It should be noted that the current traffic-light protocol for guiding hydraulic-fracturing operations relies on real-time occurrence of seismicity, and is thus reactive and a posteriori^{62,63}. Also, current approaches in estimating maximum magnitudes of induced earthquakes based on either injection volume²⁰ or assumed magnitude jumps^{63,64} are empirical or statistical. In those risk evaluation models, regional velocity and structural characteristics of a hydraulic-fracturing site are not exploited in evaluating the seismic potentials. Therefore, strategies for mitigating fluid injection-induced seismicity such as the traffic-light protocol can be combined with

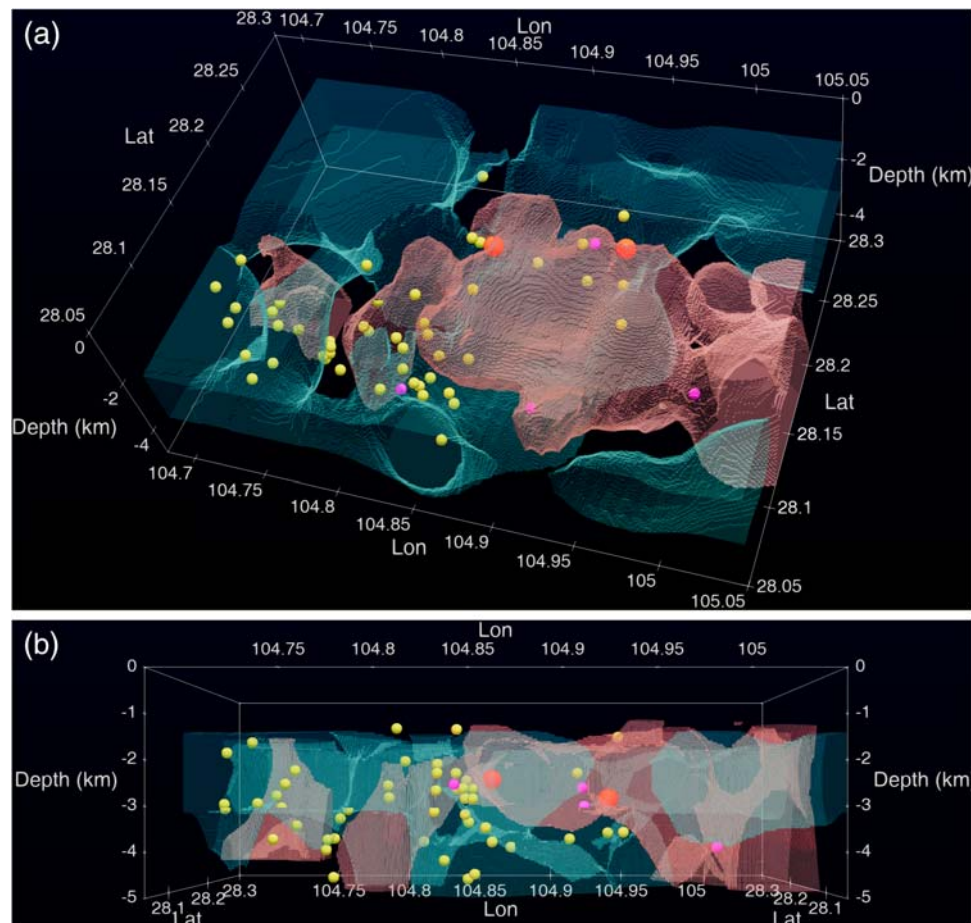


Fig. 5 Regional seismic potential assessment. **a** 3D relative higher-velocity (light blue, > 3% positive anomaly) and lower-velocity (light red, > 3% negative anomaly) anomalies sculpted from the inverted shear-wave velocity model from ANT as shown in Fig. 2. The yellow balls indicate the hypocenters of the earthquakes with $M_L \geq 3$ which occurred between 2015 and 2019, and the two damaging Xingwen M_L 5.7 and the Gongxian M_L 5.3 earthquakes are marked by the orange balls. The 4 magenta balls represent more recent earthquakes with $M_L \geq 4$ occurring after 2019. **b** The side view of **(a)** looking from south.

subsurface structural characteristics to better guide hydraulic fracturing: for regions with potential asperities for moderate to major earthquakes, the magnitude threshold should be set more conservative to avoid unexpected magnitude jumps^{63,64}. This geological susceptibility evaluation model should be combined with other risk models based on HF parameters such as the pumping pressure and the injection rate^{43,65}, or damaging impacts^{66,67} to better evaluate seismic risks in a way similar to the process-based approach⁶⁸.

In this study, we propose to evaluate susceptible areas of moderate to strong earthquakes potentially induced by HF for shale gas development based on the distribution of high-velocity anomalies above and below the target shale formations. Since many preexisting faults and weak zones could be elusive in the 3D active seismic surveys, high-resolution velocity models from ANT and other passive seismic studies can be combined to indicate the rupturing areas and maximum magnitudes of potentially induced moderate to strong earthquakes. We believe such a structure-based susceptibility evaluation approach can be used not only in the Changning-Zhaotong shale gas field, but also in many other hydraulic fracturing sites to avoid inducing damaging earthquakes.

Methods

Summary of seismic monitoring networks and their uses in the analyses. We provide a brief summary of the seismic networks and corresponding datasets used

in our study (Supplementary Fig. 22). In total, three seismic networks with different instrument types, deployment periods and station intervals in this region are used, including a dense array, a local network and a national broadband network (Fig. 1b, d). The two-phased temporary dense arrays consisting of 336 5 Hz SmartSolo and Zland nodal stations in total were deployed by the University of Science and Technology of China with an average spacing of about 1.5 km (monitoring between 28 Feb. 2019 and 8 May 2019, black triangles in the inset in Fig. 1d). The first phase of the dense array consisting of 187 short-period seismic nodal stations was deployed from 28 February, 2019 to 3 April, 2019, and then retrieved for battery charge. The second phase of the dense array consisting of 149 stations was deployed from April 4th to May 6th. In total, the two-phased arrays covered about 800 km², including the Changning-Zhaotong shale gas blocks and their adjacent areas for future development (White boxes in Fig. 1). The three-component, 5 Hz SmartSolo and Zland nodal stations with almost identical instrument responses were deployed in an alternated pattern. The sampling frequency for all the nodes is set to 500 Hz or 2 ms.

The local network was deployed by China Earthquake Networks Center and managed first by the Yibin Earthquake Prevention and Disaster Reduction Administration between Feb. 2015 and Jul. 2019 and then by the Earthquake Networks Center of Sichuan Earthquake Administration between Aug. 2019 and Dec. 2020. The local network consists of 21 stations, including 6 broadband stations of CMG-3ESPC and CMG-40T, and 15 short-period stations of FSS-3M and DS-4A (monitoring since Feb. 2015, cyan triangles in Fig. 1d). The national broadband seismic network consists of permanent stations of various types (Fig. 1b).

The temporary dense arrays recorded at 500 Hz in the field, and later the data were resampled to 100 Hz to facilitate data processing, whereas the local and national networks recorded at 200 Hz and 100 Hz in the field, respectively. Using the data recorded by the temporary dense array, we constructed a 3D shear wave velocity model using ambient noise surface wave tomography (Figs. 2, 5) and detected ~8000 microearthquakes in the C-Z field, including two $M_L > 3.0$ moderate earthquakes (Fig. 4) with well constrained depths. Using the local network, about

26,000 earthquakes ($M_L 0 - M_L 5.7$) including 53 $M_L \geq 3.0$ moderate to strong earthquakes (Fig. 1d) were detected and located (Fig. 2). The moment tensors of those 53 $M_L \geq 3.0$ earthquakes and the dynamic rupturing processes of the two $M_L > 5.0$ earthquakes were determined using the waveform data from both the local and the national broadband networks.

Ambient noise tomography. The Rayleigh wave phase velocity dispersion curves are retrieved from continuous ambient noise recordings with the two-station cross-correlation method⁶⁹ (Supplementary Method 1). The bin stacked cross-correlation functions are shown in Supplementary Fig. 2. The direct inversion method⁷⁰ is then used to invert dispersion data for the regional 3-D S-wave velocity structure with 8290 manually picked phase velocity dispersion curves in total. The direct inversion method updates the ray paths and corresponding sensitivity kernels using the fast-marching method⁷¹ at each iteration, and improves the accuracy of surface wave tomography in complex media.

The initial velocity model used for the direct surface wave inversion is estimated from the average curve of all dispersion curves using an empirical relationship⁷⁰ (Supplementary Fig. 3). The sensitivity analysis of the initial model in Supplementary Fig. 3 shows that the Rayleigh wave at period $T = 0.5$ s is sensitive to V_s at about 0.5 km in depth, and the structures at 7 km in depth is constrained by dispersion data at period $T = 5.0$ s, indicating that the target V_s structure in the upper 5 km should be well constrained and recovered by the extracted phase dispersion data within $0.5 \leq T \leq 5.0$ s. The model is represented by 3D grid nodes with grid intervals of ~ 1 km in the horizontal directions and ~ 0.5 km in the vertical direction. The checkerboard test shows that the resolution of the inverted model can reach up to 2 km horizontally and the first three anomaly layers can be recovered well in the central part shallower than 5 km (Supplementary Method 2, Supplementary Fig. 4). The ray paths are statistically illustrated as density map in Supplementary Fig. 4 which reveals high coverage in the central part where these moderate earthquakes located. The mean-squares surface wave travel times residuals at different periods decrease from 0.409 s to 0.295 s, and the mean also drops from 0.143 s to 0.012 s after inversion. See more details in the Supplementary.

Earthquake location using picked traveltimes. Two earthquake catalogs were obtained from the local network (8 Feb., 2015 to 31 Dec., 2020) and the temporary dense array (28 Feb., 2019 to 8 May, 2019), respectively. Through manual event detection in the continuous waveforms and subsequent phase arrival picking by analysts, about 26,000 earthquakes ($M_L 0 - M_L 5.7$) within the C-Z shale gas field and its surrounding areas (104.67° to 105.10° in longitude, 28.00° to 28.30° in latitude) were located by the local network consisting of 21 stations. For these 53 $M_L \geq 3.0$ earthquakes in this catalog, we carefully repicked the P- and S-arrivals manually from the stations with relatively small epicentral distances (e.g., Supplementary Fig. 7) and removed the stations with large traveltime residuals to further improve location accuracy. For the seismic data collected by the temporary two-phased dense arrays, we first used the Kurtosis values⁷² of seismic traces to automatically detect events in the continuous waveforms. About 8000 earthquakes ($M_L - 1.0$ to $M_L 3.7$) were initially detected and then checked again manually one by one. Subsequently, human analysts carefully picked 500,000 P-arrivals and 420,000 S-arrivals for the detected events, which were then first located with NonLinLoc⁷³ using the absolute arrival times, and then relocated with the double-difference method⁷⁴ for better accuracy. The layered model in Supplementary Fig. 3 was used for locating the events monitored by the two-phased dense arrays and the 53 $M_L \geq 3.0$ earthquakes monitored by the local network.

The average location uncertainties for those earthquakes monitored by the local network and the dense arrays are about 0.36 km and 0.13 km, respectively, as estimated by the double-difference method from the traveltime residuals⁷⁴.

Moment tensor inversion using full waveform matching. We used the full waveform matching method^{75,76} to invert for the focal mechanisms of these 53 $M_L \geq 3.0$ earthquakes (Fig. 2, Table S1) in the C-Z area using waveforms up to a few Hertz from the local network and from some surrounding permanent broadband stations in the national seismic network (white rhombus in Fig. 1b) operated by China Earthquake Administration (Fig. 1). The instrumental responses of all used stations were carefully removed. The layered velocity model used for locating these earthquakes was also used for synthesizing the Green's functions. The objective function for moment tensor inversion includes four terms to compare the differences between the observed and synthetic data in P-wave first motion polarities, L2 norm of the waveform matching, cross-correlation coefficients between the observed and synthetic waveforms, as well as the average S/P amplitude ratios:

$$\begin{aligned} \text{maximize}(J(x, y, z, \Phi, \delta, \lambda, t_s)) = & \sum_{n=1}^N \sum_{j=1}^3 \{ \alpha_1 \max(\tilde{d}_j^n \otimes \tilde{v}_j^n) - \alpha_2 \|\tilde{d}_j^n - \tilde{v}_j^n\|_2 \\ & + \alpha_3 f(\text{pol}(\tilde{d}_j^n), \text{pol}(\tilde{v}_j^n)) \\ & + \alpha_4 h \left(\text{rat} \left(\frac{S(d_j^n)}{P(d_j^n)} \right), \text{rat} \left(\frac{S(v_j^n)}{P(v_j^n)} \right) \right) \}, \end{aligned} \quad (1)$$

where x, y , and z denote the event hypocenter that will be redetermined by waveform matching, Φ, δ, λ are the strike, dip and rake of an earthquake, t_s is the

time shift that gives the largest cross-correlation value between the observed and synthetic seismograms; \tilde{d}_j^n is the normalized observed waveform and \tilde{v}_j^n is the normalized synthetic waveform, α_1 through α_4 are the weights, pol is the polarity evaluation function, and f penalizes the discrepancy; rat calculates the ratio between the S- and P-waves of either the observed or the synthetic data, and h penalizes the ratio discrepancy. Since the site effect sometimes cannot be neglected for relatively high-frequency waveforms, the waveform at each station is normalized by its energy for stability concerns. The method utilizes much information in the waveforms, and can yield stable source mechanism solutions for smaller earthquakes. Thus, our source mechanism inversion method does not yield moment magnitudes directly. Instead, we use the moment magnitudes from literature if they are available, or the local magnitude when the moment magnitude is not available.

Based on the regional layered model in Supplementary Fig. 3, we first calculated the waveform Green's functions from all the earthquake epicenters in the depth range of 0–10 km at an interval of 0.5 km to the regional broadband stations using the DWN method (Bouchon, 2003). Stations in the close proximity to the larger events with saturated waveforms are not used. After removals of the instrumental responses, means and trends of the waveforms, the seismic waveforms used for inversion are typically filtered between 0.05 Hz and 0.2 Hz for earthquakes with larger magnitudes and between 0.2 Hz and 2 Hz for those smaller ones. We adjusted the weights ($\alpha_1, \alpha_2, \alpha_3, \alpha_4$ in Eq. 1) of the different terms in the object function (P-wave first motion polarity, L2 norm of the waveform matching, cross-correlation coefficient between the observed and synthetic waveforms, and the average S/P amplitude ratio, respectively) to balance the contributions from each term for stable inversion results. For most events, the weights are set to 1, 1, 0.5 and 0.01 for $\alpha_1, \alpha_2, \alpha_3, \alpha_4$, respectively. See more details about uncertainty evaluations for focal mechanism solutions and the centroid depths in Supplementary Method 3.

Spatial-temporal rupture imaging based on finite-fault rupture inversion. We determined the source rupture processes of the Xingwen $M_L 5.7$ and Gongxian $M_L 5.3$ earthquakes using the finite-fault rupture inversion^{77,78}. The joint inversion with seismic and geodetic data is:

$$\begin{bmatrix} \lambda_0 U \\ 0 \\ 0 \\ 0 \\ \lambda_s Q \\ 0 \end{bmatrix} = \begin{bmatrix} \lambda_0 \begin{bmatrix} G_x & G_y \end{bmatrix} \\ \lambda_1 \begin{bmatrix} D & 0 \\ 0 & D \end{bmatrix} \\ \lambda_2 \begin{bmatrix} T & 0 \\ 0 & T \end{bmatrix} \\ \lambda_3 \begin{bmatrix} Z & 0 \\ 0 & Z \end{bmatrix} \\ \lambda_s \begin{bmatrix} K_x & K_y \\ \lambda_4 \begin{bmatrix} D & 0 \\ 0 & D \end{bmatrix} \end{bmatrix} \end{bmatrix} \begin{bmatrix} m_x \\ m_y \end{bmatrix}, \quad (2)$$

where U and Q represent the observed seismic waveforms and InSAR data, respectively; m are the unknown vectors to be solved, which describes the time history of slip-rate amplitudes and slip angles of all sub-faults on the fault plane; G and K denote the Green's functions for seismic waveforms and surface deformations, respectively; D and T are spatial and temporal smoothness matrices, respectively; Z is the matrix for minimizing the scalar moment, and λ_1 through λ_4 represent the corresponding weights for each term.

Given the source mechanism or fault geometry and the initiation point, the near-field seismic waveforms (Supplementary Figs. 16a, b) together with the InSAR data (see processing details in Supplementary Method 4) are used to invert for the fault rupture process without any assumption for the shapes of the sub-fault source time functions. For the calculations of the waveform Green's functions in finite-fault inversion, we used the method developed by Wang (1999), which is very efficient in computing high-frequency waveforms. For modelling the surface deformation, we used the elastic half-space dislocation theory (Okada, 1985). To improve the stability of the result, appropriate constraints were carefully applied, including a spatiotemporal smooth constraint, limits for the maximum rupture velocity and rupturing durations of the sub-faults. The inverted rupturing process, seismic waveform matching and surface deformation fitting are shown in Supplementary Fig. 16b for the Xingwen $M_L 5.7$ earthquake, and in Supplementary Fig. 16c for the Gongxian $M_L 5.3$ earthquake. Some large-amplitude shear waves at stations in close proximity to those two strong earthquakes are clipped. Using the projection onto convex sets (POCS) method⁴⁶, we reconstructed the truncated waveforms by alternating between iterative and progressive constraints of the frequency spectra and the temporal waveforms. Overly clipped waveforms are rejected if the peak amplitudes of the truncated waveform are less than 40% of the peak amplitudes of reconstructed waveforms to warrant the restoration error is less than 5%⁷⁷. In Supplementary Fig. 17, it is found that the reconstructed seismograms are identical with the raw ones for the unclipped parts (i.e., small amplitudes). Also, we can see that before and after the reconstruction the spread of the spectra are in general quite similar.

The surface deformation obtained from the InSAR data for the Gongxian $M_L 5.3$ earthquake is used for finite fault inversion, but the surface deformation for the Xingwen $M_L 5.7$ earthquake is not used since it is suspected to be heavily contaminated by a mountain collapse associated with the earthquake, as our field surveys found (Supplementary Fig. 18). Also, no obvious HF-related surface deformations were observed within two months prior to the Gongxian $M_L 5.3$ earthquakes⁷⁹. Thus, the interferograms used in our study should contain no or negligible deformations related to the chronicle HF developments in the unconventional field and should mostly characterize the coseismic deformations related to the earthquake rupturing process. See more details in the supplementary section “Details for the finite fault rupture inversion.”

Slip tendency. We invert the 53 focal mechanisms (Method-Moment tensor inversion using full waveform matching) for the stress state in the Changning-Zhaotong shale gas field using the iterative method⁸⁰ which avoids ambiguity in identifying the fault planes in focal mechanisms. The new method iteratively determines the fault planes of the focal mechanisms using the fault instability constraint and invert for the stress state until a stable stress solution is obtained. The inverted result shows that the tectonic stress field in this area is very close to the thrust type (Supplementary Fig. 12). Assuming that σ_3 is the lithostatic pressure ($\sigma_3 = \rho g z = 3000 \text{ kg} \cdot \text{m}^{-3} \cdot 10 \text{ N} \cdot \text{kg}^{-1} \cdot 2000 \text{ m} = 60 \text{ MPa}$), $\sigma_1 - \sigma_2 = 22 \text{ MPa}$ ²⁹ and the shape ratio $R = 0.877$, we can estimate the magnitudes of the three principal stresses are 85, 63 and 60 MPa at 2 km depth, respectively. Using the orientation and magnitude of the stress state, we can also calculate the normal stress σ_n , the shear stress σ_s on a given/receiver fault, as well as the slip tendency $ST = \sigma_s / \sigma_n$ (Supplementary Fig. 12).

Static coulomb stress calculation. Using the Coulomb software⁸¹, we calculated the static Coulomb stress change caused by the $M_L 3.0$ earthquake occurring on 15 December, 2018. The strike/dip/rake for the source fault is set as $360^\circ/85^\circ/-30^\circ$ at the focal depth of 3.0 km, and the geometry of the receiver fault is assumed to be $345^\circ/90^\circ/0^\circ$ for strike/dip/rake (Table S1). The source fault size (0.5 km by 0.5 km for $M_L 3.0$ earthquake) used in the Coulomb software is estimated from the empirical relationship⁵⁰, and the friction coefficient is assumed to be 0.5. The calculation is performed in a half-space elastic model for simplification. The result shown in Supplementary Fig. 19 indicates that the stress perturbation from the $M_L 3.0$ earthquake on the Xingwen $M_L 5.7$ earthquake is insignificant for triggering the Xingwen $M_L 5.7$ mainshock.

Data availability

The dispersion curves for ambient noise tomography, the inverted shear wave velocity model, the earthquake catalogs monitored by the two-phased arrays and the sparse permanent network, as well as the waveforms data of the 53 moderate to strong earthquakes are available at <https://zenodo.org/record/6474345/YmDXP8YzZhE>. The 2D active seismic profile is from Lu et al. (2021). The InSAR data can be downloaded at <https://scihub.copernicus.eu>.

Code availability

The codes for the extraction and direct inversion of surface wave dispersion curves are available from <http://yaolab.ustc.edu.cn/resources.php?i=28>; The codes for the earthquake relocation can be downloaded at <http://alomax.free.fr/nlloc> (NonLinLoc) and <https://www.ldeo.columbia.edu/~felixw/hypoDD.html> (HypoDD); The code for finite-fault rupture inversion of earthquakes is provided by Yong Zhang at Peking University. The codes for full waveform inversion of earthquake source mechanisms is developed by JL at the University of Sciences and Technology of China and can be provided upon request. The codes for inverting for stress field and calculating static Coulomb stress perturbation are available at <http://www.ig.cas.cz/stress-inverse> and <https://www.usgs.gov/node/279387>, respectively. The InSAR Scientific Computing Environment (ISCE) software developed at JPL/Caltech (<https://github.com/isce-framework/isce2>) are used to processed the remote sensing data. Figures 1–4 are made by the Generic Mapping Tools which can be downloaded at <https://www.generic-mapping-tools.org/>, and Fig. 5 is made by Paraview which is open source and can be downloaded at <https://www.paraview.org/>.

Received: 28 August 2022; Accepted: 17 May 2023;

Published online: 29 May 2023

References

- Ellsworth, W. L. Injection-induced earthquakes. *Science* **341**, 1225942 (2013).
- Shapiro, S. A. *Fluid-Induced Seismicity* (Cambridge Univ. Press, 2015).
- Bao, X. W. & Eaton, D. W. Fault activation by hydraulic fracturing in western Canada. *Science* **354**, 1406–1409 (2016).

- Deng, K., Liu, Y. J. & Harrington, R. M. Poroelastic stress triggering of the December 2013 Crooked Lake, Alberta, induced seismicity sequence. *Geophys. Res. Lett.* **43**, 8482–8491 (2016).
- Lei, X. L. et al. Fault reactivation and earthquakes with magnitudes of up to $M_w 4.7$ induced by shale-gas hydraulic fracturing in Sichuan Basin, China. *Sci. Rep.* **7**, 7971 (2017).
- Van der Baan, M. & Calixto, F. J. Human-induced seismicity and large-scale hydrocarbon production in the USA and Canada. *Geochem. Geophys.* **18**, 2467–2485 (2017).
- Foulger, G. R., Wilson, M. P., Gluyas, J. G., Julian, B. R. & Davies, R. J. Global review of human-induced earthquakes. *Earth Sci. Rev.* **178**, 438–514 (2018).
- Goebel, T. H. W. & Brodsky, E. E. The spatial footprint of injection wells in a global compilation of induced earthquake sequences. *Science* **361**, 899–903 (2018).
- Schultz, R., Atkinson, G., Eaton, D. W., Gu, Y. J. & Kao, H. Hydraulic fracturing volume is associated with induced earthquake productivity in the Duvernay play. *Science* **359**, 304–308 (2018).
- Bhattacharya, P. & Viesca, R. C. Fluid-induced aseismic fault slip outpaces pore-fluid migration. *Science* **364**, 464–468 (2019).
- Eyre, T. S. et al. The role of aseismic slip in hydraulic fracturing-induced seismicity. *Sci. Adv.* **5**, eaav7172 (2019).
- Zoback, M. D. & Kohli, A. H. *Unconventional Reservoir Geomechanics* (Cambridge Univ. Press, 2019).
- Horton, S. Disposal of hydrofracturing waste fluid by injection into subsurface aquifers triggers earthquake swarm in central Arkansas with potential for damaging earthquake. *Seismol. Res. Lett.* **83**, 250–260 (2012).
- Keranen, K. M., Savage, H. M., Abers, G. A. & Cochran, E. S. Potentially induced earthquakes in Oklahoma, USA: Links between wastewater injection and the 2011 $M_w 5.7$ earthquake sequence. *Geology* **41**, 699–702 (2013).
- Weingarten, M., Ge, S., Godt, J. W., Bekins, B. A. & Rubinstein, J. L. High-rate injection is associated with the increase in US mid-continent seismicity. *Science* **348**, 1336–1340 (2015).
- Atkinson, G. M. et al. Hydraulic fracturing and seismicity in the Western Canada Sedimentary Basin. *Seismol. Res. Lett.* **87**, 631–647 (2016).
- Yeck, W. L. et al. Far-field pressurization likely caused one of the largest injection induced earthquakes by reactivating a large preexisting basement fault structure. *Geophys. Res. Lett.* **43**, 10198–10207 (2016).
- Schultz, R., Wang, R. J., Gu, Y. J., Haug, K. & Atkinson, G. A seismological overview of the induced earthquakes in the Duvernay play near Fox Creek, Alberta. *J. Geophys. Res.: Solid Earth* **122**, 492–505 (2017).
- Konstantinovskaya, E. et al. Lateral fluid propagation and strike slip fault reactivation related to hydraulic fracturing and induced seismicity in the Duvernay formation, Fox Creek area, Alberta. *Geophys. J. Int.* **227**, 518–543 (2021).
- McGarr, A. Maximum magnitude earthquakes induced by fluid injection. *J. Geophys. Res.: Solid Earth* **119**, 1008–1019 (2014).
- Galis, M., Ampuero, J. P., Mai, P. M. & Cappa, F. Induced seismicity provides insight into why earthquake ruptures stop. *Sci. Adv.* **3**, eaap7528 (2017).
- Ellsworth, W. L., Giardini, D., Townend, J., Ge, S. M. & Shimamoto, T. Triggering of the Pohang, Korea, Earthquake ($M_w 5.5$) by Enhanced Geothermal System Stimulation. *Seismol. Res. Lett.* **90**, 1844–1858 (2019).
- Shapiro, S. A., Kim, K. H. & Ree, J. H. Magnitude and nucleation time of the 2017 Pohang Earthquake point to its predictable artificial triggering. *Nat. commun.* **12**, 1–9 (2021).
- BC Oil and Gas Commission. *Investigation of observed seismicity in the Montney trend*. (2014).
- Holland, A. A. Preliminary fault map of Oklahoma. *Okla. Geol. Surv. Open File Rept.* OF3-2015 (2015).
- Eaton, D. W. et al. Induced Seismicity Characterization during Hydraulic-Fracture Monitoring with a Shallow-Wellbore Geophone Array and Broadband Sensors. *Seismol. Res. Lett.* **89**, 1641–1651 (2018).
- Kolawole, F. et al. The susceptibility of Oklahoma's basement to seismic reactivation. *Nat. Geosci.* **12**, 839–844 (2019).
- Schoenball, M. & Ellsworth, W. L. Waveform-relocated earthquake catalog for Oklahoma and southern Kansas illuminates the regional fault network. *Seismol. Res. Lett.* **88**, 1252–1258 (2017).
- Lei, X., Wang, Z. & Su, J. Possible link between long-term and short-term water injections and earthquakes in salt mine and shale gas site in Changning, South Sichuan Basin, China. *Earth Planet. Phys.* **3**, 510–525 (2019).
- Meng, L. Y., McGarr, A., Zhou, L. Q. & Zang, Y. An investigation of seismicity induced by hydraulic fracturing in the Sichuan Basin of China Based on Data from a temporary seismic network. *Bull. Seismol. Soc. Am.* **109**, 348–357 (2019).
- Xu, Z. Y., Jiang, S., Yao, G. S., Liang, X. & Xiong, S. Y. Tectonic and depositional setting of the lower Cambrian and lower Silurian marine shales in the Yangtze Platform, South China: Implications for shale gas exploration and production. *J. Asian. Earth. Sci.* **170**, 1–19 (2019).

32. Lei, X., Su, J. & Wang, Z. Growing seismicity in the Sichuan Basin and its association with industrial activities. *Sci. China: Earth Sci.* **63**, 1633–1660 (2020).
33. Tan, Y. Y. et al. Hydraulic fracturing induced seismicity in the southern Sichuan Basin due to fluid diffusion inferred from seismic and injection data analysis. *Geophys. Res. Lett.* **47**, e2019GL084885 (2020).
34. Lei, X. L., Wang, Z. W. & Su, J. R. The December 2018 M-L 5.7 and January 2019 M-L 5.3 earthquakes in south Sichuan basin induced by shale gas hydraulic fracturing. *Seismol. Res. Lett.* **90**, 2092–2093 (2019).
35. Atkinson, G. M., Eaton, D. W. & Igonin, N. Developments in understanding seismicity triggered by hydraulic fracturing. *Nat. Rev. Earth. Env.* **1**, 264–277 (2020).
36. Lu, R. Q. et al. Seismogenic faults of the changing earthquake sequence constrained by high-resolution seismic profiles in the southwestern Sichuan Basin, China. *Seismol. Res. Lett.* **92**, 3757–3766 (2021).
37. He, D. F. et al. Tectonic and geological setting of the earthquake hazards in the changing shale gas development zone, Sichuan Basin, SW China. *Pet. Explor. Dev.* **46**, 1051–1064 (2019).
38. Anyiam, U. O. Improved Crustal Structure, Seismicity, Stress and Pore Pressure Characterization of Changning-Xingwen Shale Gas and Salt Mine Areas, Sichuan Basin Ph. D. thesis, University of Science and Technology of China (2022).
39. Qiu, Z. et al. Discussion on characteristics and controlling factors of differential enrichment of Wufeng-Longmaxi formations shale gas in South China. *Nat. Gas Geosci.* **31**, 163–175 (2020).
40. Heidbach, O., Rajabi, M., Reiter, K., Ziegler, M. & Team, W. World Stress Map Database Release 2016. *GFZ Data Services* **10**, 1 (2016).
41. Zhu, L. & Ben-Zion, Y. Parametrization of general seismic potency and moment tensors for source inversion of seismic waveform data. *Geophys. J. Int.* **194**, 839–843 (2013).
42. Husen, S. & Hardebeck, J. Earthquake Location Accuracy. *CORSSA* (2010).
43. An, M. K. et al. Stress perturbation caused by multistage hydraulic fracturing: Implications for deep fault reactivation. *Int. J. Rock. Mech. Min.* **141**, 104704 (2021).
44. Woo, J. U. et al. An In-depth seismological analysis revealing a causal Link between the 2017 M-W 5.5 Pohang earthquake and EGS project. *J. Geophys. Res.: Solid Earth* **124**, 13060–13078 (2019).
45. Kim, K. H. et al. The 2017 ML 5.4 Pohang earthquake sequence, Korea, recorded by a dense seismic network. *Tectonophysics* **774**, 228306 (2020).
46. Zhang, J. H. et al. Restoration of clipped seismic waveforms using projection onto convex sets method. *Sci. Rep.* **6**, 1–10 (2016).
47. Pei, S. P., Zhang, H. J., Su, J. R. & Cui, Z. X. Ductile gap between the Wenchuan and Lushan earthquakes revealed from the two-dimensional Pg seismic tomography. *Sci. Rep.* **4**, 6489 (2014).
48. Wang, Z., Su, J. R., Liu, C. X. & Cai, X. L. New insights into the generation of the 2013 Lushan earthquake (M-s 7.0), China. *J. Geophys. Res.: Solid Earth* **120**, 3507–3526 (2015).
49. Sun, Q. et al. Structure-controlled asperities of the 1920 Haiyuan M8.5 and 1927 Gulang M8 earthquakes, NE Tibet, China, revealed by high-resolution seismic tomography. *Sci. Rep.* **11**, 1–8 (2021).
50. Wells, D. L. & Coppersmith, K. J. New empirical relationships among magnitude, rupture length, rupture width, rupture area, and surface displacement. *Bull. Seismol. Soc. Am.* **84**, 974–1002 (1994).
51. Galloway, E., Hauck, T., Corlett, H., Panà, D. & Schultz, R. Faults and associated karst collapse suggest conduits for fluid flow that influence hydraulic fracturing-induced seismicity. *PNAS* **115**, E10003–E10012 (2018).
52. Chen, J. Y., Verberne, B. A. & Spiers, C. J. Interseismic re-strengthening and stabilization of carbonate faults by “non-Dieterich” healing under hydrothermal conditions. *Earth Planet. Sci. Lett.* **423**, 1–12 (2015).
53. An, M. K., Zhang, F. S., Chen, Z. W., Elsworth, D. & Zhang, L. Y. Temperature and fluid pressurization effects on frictional stability of shale faults reactivated by hydraulic fracturing in the changing block, southwest China. *J. Geophys. Res.: Solid Earth* **125**, e2020JB019584 (2020).
54. Zou, C. et al. Geological characteristics, main challenges and future prospect of shale gas. *Nat. Gas Geosci.* **2**, 273–288 (2017).
55. Wang, Z., Fukao, Y. & Pei, S. P. Structural control of rupturing of the Mw7.9 2008 Wenchuan earthquake, China. *Earth Planet. Sci. Lett.* **279**, 131–138 (2009).
56. Romano, F. et al. Structural control on the Tohoku earthquake rupture process investigated by 3D FEM, tsunami and geodetic data. *Sci. Rep.* **4**, 5631 (2014).
57. Chiarabba, C., De Gori, P., Cattaneo, M., Spallarossa, D. & Segou, M. Faults geometry and the role of fluids in the 2016–2017 central Italy seismic sequence. *Geophys. Res. Lett.* **45**, 6963–6971 (2018).
58. Agostinetti, N. P., Giacomuzzi, G. & Chiarabba, C. Across-fault velocity gradients and slip behavior of the San Andreas Fault near Parkfield. *Geophys. Res. Lett.* **47**, e2019GL084480 (2020).
59. Pei, S. P., Peng, Z. G. & Chen, X. W. Locations of Injection-Induced earthquakes in Oklahoma controlled by crustal structures. *J. Geophys. Res.: Solid Earth* **123**, 2332–2344 (2018).
60. Schultz, R. et al. Linking fossil reefs with earthquakes: Geologic insight to where induced seismicity occurs in Alberta. *Geophys. Res. Lett.* **43**, 2534–2542 (2016).
61. Schultz, R. et al. Hydraulic fracturing-induced seismicity. *Rev. Geophys.* **58**, e2019RG000695 (2020).
62. Kao, H., Visser, R., Smith, B. & Venables, S. Performance assessment of the induced seismicity traffic light protocol for northeastern British Columbia and western Alberta. *Lead. Edge* **37**, 117–126 (2018).
63. Verdon, J. P. & Bommer, J. J. Green, yellow, red, or out of the blue? An assessment of traffic light schemes to mitigate the impact of hydraulic fracturing-induced seismicity. *J. Seismol.* **25**, 301–326 (2021).
64. Schultz, R., Ellsworth, W. L. & Beroza, G. C. Statistical bounds on how induced seismicity stops. *Sci. Rep.* **12**, 1184 (2022).
65. Zhu, J. B. et al. Controlling induced earthquake magnitude by cycled fluid injection. *Geophys. Res. Lett.* **48**, e2021GL092885 (2021).
66. Bommer, J. J., Crowley, H. & Pinho, R. A risk-mitigation approach to the management of induced seismicity. *J. Seismol.* **19**, 623–646 (2015).
67. Schultz, R., Beroza, G. C. & Ellsworth, W. L. A risk-based approach for managing hydraulic fracturing-induced seismicity. *Science* **372**, 504–507 (2021).
68. Hager, B. H. et al. A process-based approach to understanding and managing triggered seismicity. *Nature* **595**, 684–689 (2021).
69. Yao, H. J., van der Hilst, R. D. & de Hoop, M. V. Surface-wave array tomography in SE Tibet from ambient seismic noise and two-station analysis - I. Phase velocity maps. *Geophys. J. Int.* **166**, 732–744 (2020).
70. Fang, H. J., Yao, H. J., Zhang, H. J., Huang, Y. C. & van der Hilst, R. D. Direct inversion of surface wave dispersion for three-dimensional shallow crustal structure based on ray tracing: methodology and application. *Geophys. J. Int.* **201**, 1251–1263 (2015).
71. Rawlinson, N. & Sambridge, M. Wave front evolution in strongly heterogeneous layered media using the fast marching method. *Geophys. J. Int.* **156**, 631–647 (2004).
72. Saragiotis, C. D., Hadjileontiadis, L. J. & Panas, S. M. PAI-S/K: A robust automatic seismic P phase arrival identification scheme. *IEEE T. Geosci. Remote.* **40**, 1395–1404 (2002).
73. Lomax, A., Virieux, J., Volant, P. & Berge-Thierry, C. in *Advances in Seismic Event Location* 101–134 (Springer, 2000).
74. Zhang, H. J. & Thurber, C. H. Double-difference tomography: The method and its application to the Hayward Fault, California. *Bull. Seismol. Soc. Am.* **93**, 1875–1889 (2003).
75. Li, J. L., Kuleli, H. S., Zhang, H. J. & Toksoz, M. N. Focal mechanism determination of induced microearthquakes in an oil field using full waveforms from shallow and deep seismic networks. *Geophysics* **76**, Wc87–Wc101 (2011).
76. Li, J. L., Zhang, H. J., Kuleli, H. S. & Toksoz, M. N. Focal mechanism determination using high-frequency waveform matching and its application to small magnitude induced earthquakes. *Geophys. J. Int.* **184**, 1261–1274 (2011).
77. Zhang, Y. et al. The 2009 L'Aquila MW 6.3 earthquake: A new technique to locate the hypocentre in the joint inversion of earthquake rupture process. *Geophys. J. Int.* **191**, 1417–1426 (2012).
78. Zhang, Y. et al. Automatic imaging of earthquake rupture processes by iterative deconvolution and stacking of high-rate GPS and strong motion seismograms. *J. Geophys. Res.: Solid Earth* **119**, 5633–5650 (2014).
79. Wang, S. et al. Three Mw ≥ 4.7 earthquakes within the changing (China) shale gas field ruptured shallow faults intersecting with hydraulic fracturing wells. *J. Geophys. Res.: Solid Earth* **127**, e2021JB022946 (2022).
80. Vavryčuk, V. Iterative joint inversion for stress and fault orientations from focal mechanisms. *Geophys. J. Int.* **199**, 69–77 (2014).
81. Toda, S., Stein, R. S., Richards-Dinger, K. & Bozkurt, S. B. Forecasting the evolution of seismicity in Southern California: Animations built on earthquake stress transfer. *J. Geophys. Res.: Solid Earth* **110**, B05S16 (2005).

Acknowledgements

We thank JinRong Su and Guixi Yi at the Sichuan Earthquake Administration for providing some of the earthquake waveform data from the local network, and Prof. Serge A. Shapiro for providing many helpful suggestions to improve this study. We thank Yue Wang and Zhe Wang for their contributions in manually picking the P- and S-arrivals of the microseismic events monitored by the two-phased dense arrays. We thank Dr. Kezhen Zuo for providing the additional earthquake catalog in 2020 for the Changning region from the local network. This research has been funded by the National Science Foundation of China under Grants U2139204, 41874048 and 41974068, and by National R&D Program of China under grant 2022YFF0800701.

Author contributions

J.L. and H.Z. initiated and supervised the research. J.L., J.X. and H.Z. analyzed the results and wrote the manuscript; J.X. inverted for the 3D shear wave velocity model; W.Y. relocated all the earthquakes; C.G. and Z.L. inverted for the source mechanisms of the moderate to strong earthquakes, the local stress field and slip tendency; S.M. constructed the spatial and temporal rupture model of the two strong earthquakes; L.M. and Y.Z.

provided the earthquake catalog using the sparse permanent network; J.S. processed the InSAR data and provided the surface deformation for the Gongxian M_L 5.3 earthquake; Y.T., F.Z. and R.L. are involved in interpreting the distribution of the earthquakes and their association with the local geology; All authors reviewed the manuscript.

Competing interests

The authors declare no competing interests.

Additional information

Supplementary information The online version contains supplementary material available at <https://doi.org/10.1038/s43247-023-00854-x>.

Correspondence and requests for materials should be addressed to Junlun Li or Haijiang Zhang.

Peer review information *Communications Earth & Environment* thanks Ryan Schultz and the other, anonymous, reviewer(s) for their contribution to the peer review of this work. Primary Handling Editors: Sylvain Barbot, Joe Aslin and Clare Davis. A peer review file is available.

Reprints and permission information is available at <http://www.nature.com/reprints>

Publisher's note Springer Nature remains neutral with regard to jurisdictional claims in published maps and institutional affiliations.



Open Access This article is licensed under a Creative Commons Attribution 4.0 International License, which permits use, sharing, adaptation, distribution and reproduction in any medium or format, as long as you give appropriate credit to the original author(s) and the source, provide a link to the Creative Commons license, and indicate if changes were made. The images or other third party material in this article are included in the article's Creative Commons license, unless indicated otherwise in a credit line to the material. If material is not included in the article's Creative Commons license and your intended use is not permitted by statutory regulation or exceeds the permitted use, you will need to obtain permission directly from the copyright holder. To view a copy of this license, visit <http://creativecommons.org/licenses/by/4.0/>.

© The Author(s) 2023